The Cryosphere Discuss., doi:10.5194/tc-2016-34, 2016
Manuscript under review for journal The Cryosphere
Published: 17 March 2016
© Author(s) 2016. CC-BY 3.0 License.

The Cryosphere Discussions
Open Access
EGU

The EUMETSAT sea ice climate record

R. T. Tonboe[1], S. Eastwood[2], T. Lavergne[2], A. M. Sørensen[2], N. Rathmann[3], G. Dybkjær[1], L. Toudal Pedersen[1], J. L. Høyer[1], S. Kern[4]
[1]Danish Meteorological Institute, Lyngbyvej 100, Copenhagen, DK-2100, Denmark
[2]Norwegian Meteorological Institute, P.O.BOX 43, Oslo, N-0313, Norway
[3]University of Copenhagen, Juliane Maries Vej 30, Copenhagen, DK-2100, Denmark
[4]University of Hamburg, Grindelberg 5, Hamburg, D-20144, Germany

Correspondence to: R. T. Tonboe (rtt@dmi.dk)

Abstract. An Arctic and Antarctic sea ice area and extent dataset has been generated by EUMETSAT's Ocean and Sea Ice Satellite Application Facility (OSISAF) using the record of American microwave radiometer data from Nimbus 7 Scanning Multichannel Microwave radiometer (SMMR) and the Defense Meteorological satellite Program (DMSP) Special Sensor Microwave/ Imager (SSM/I) and Special Sensor Microwave Imager and Sounder (SSMIS) satellite sensors. The dataset covers the period from 1978 to 2014 and updates and further developments are planned for the next phase of the project. The methodology is using: 1) numerical weather prediction (NWP) input to a radiative transfer model (RTM) for correction of the brightness temperatures for reduction of atmospheric noise, 2) dynamical algorithm tie-points to mitigate trends in residual atmospheric, sea ice and water emission characteristics and inter-sensor differences/biases, 3) and a hybrid sea ice concentration algorithm using the Bristol algorithm over ice and the Bootstrap algorithm in frequency mode over open water. A new algorithm has been developed to estimate the spatially and temporally varying sea ice concentration uncertainties. A comparison to sea ice charts from the Arctic and the Antarctic shows that ice concentrations are higher in the ice charts than estimated from the radiometer data at intermediate ice concentrations. The sea ice climate dataset is available for download at (www.osisaf.org) including documentation.

1. Introduction

The Arctic sea ice area and extent has decreased since the 1970s (Cavalieri and Parkinson, 2012). In Antarctica there are large regional differences in trends but overall the sea ice extent is increasing because of changing atmospheric circulation patterns and regional cooling (Comiso et al., 2011). The climatic trends in sea ice extent have been documented using models (Zhang and Walsh, 2006), ice charts (Rayner et al., 2003) and in particular the passive microwave data record from American satellite

The Cryosphere Discuss., doi:10.5194/tc-2016-34, 2016
Manuscript under review for journal The Cryosphere
Published: 17 March 2016
© Author(s) 2016. CC-BY 3.0 License.

microwave radiometers (Parkinson and Cavalieri, 2012; Cavalieri and Parkinson, 2012). Here the sea ice extent is defined as ice covered waters with ice concentrations derived from microwave radiometer data greater than 15% as in Parkinson and Cavalieri (2008) and at a grid resolution of 12.5 x 12.5 kilometers.

The brightness temperatures measured by the satellite radiometers at the atmospheric window channels are dominated by surface emission. However, the measured brightness temperatures are also affected by atmospheric parameters such as wind roughening of the ocean surface, water vapor and cloud liquid water (Wentz, 1983 and 1997; Andersen et al., 2006B). These parameters have trends over the observing period (Wentz et al., 2007). Even though the sensitivity to these parameters is minimized in ice concentration algorithms in general different algorithms still have different sensitivities resulting in structural uncertainties, i.e. different outcome from different algorithms using the same data (Andersen et al., 2006B).

Because of the algorithms different sensitivities to the noise, and that the noise has climatic trends, the differences are also reflected in the sea ice extent trends (Andersen et al., 2007). To minimize these artificial trends we must: 1) find algorithms with low sensitivities to the atmospheric and surface emissivity variability, 2) correct the brightness temperatures for the properties that we are able to quantify, and in particular when doing this it is important to 3) calibrate the algorithms to the actual ice and water signatures using dynamical tie-points, and finally 4) quantify the residual uncertainties. The EUMETSAT sea ice climate record (ESICR) is generated according to these principles, 1 - 4, and it is based on the Nimbus 7 Scanning Multichannel Microwave Radiometer (SMMR) (1978-1987), the Special Sensor Microwave/Imager (SSM/I) (1987-2009) and the Special Sensor Microwave Imager and Sounder (SSMIS) (2003-today) radiometer data. It uses a combination of the Bristol (Smith, 1996) and the Bootstrap (Comiso, 1986) algorithms with dynamical tie-points, explicit atmospheric correction using numerical weather prediction data for error reduction and it comes with spatially and temporally varying uncertainty estimates describing the residual uncertainties.

Uncertainty estimates are needed when the ice concentration data are compared to other data sets or when the ice concentrations are assimilated into numerical models. The mean accuracy of some of the

The Cryosphere Discuss., doi:10.5194/tc-2016-34, 2016
Manuscript under review for journal The Cryosphere
Published: 17 March 2016
© Author(s) 2016. CC-BY 3.0 License.

more common algorithms, used to compute ice concentration from SSM/I data, such as the NASA Team and Bootstrap are reported to be 1-6% in winter (Steffen and Schweiger, 1991; Emery et al., 1994; Belchansky and Douglas, 2002). The overall accuracy of the SMMR total ice concentrations is estimated to be ±7% (Gloersen et al., 1992). During summer the uncertainties are larger than during winter (Ivanova et al., 2015).

1.1 Description of the Nimbus 7 SMMR instrument and data

The SMMR instrument on board the Nimbus 7 satellite operated from October 1978 to August 1987 (Gloersen et al., 1992). The instrument had 10 channels from the six Dicke radiometers at five frequencies (6.6, 10.7, 18.0, 21.0, 37.0 GHz) and vertical and horizontal linear polarization. The across track scanning was accomplished by tilting the reflector from side to side while maintaining a constant incidence angle on the ground of about 50.2°. The scan track on the ground formed a 780 km wide arc in front of the satellite (Gloersen and Barath, 1977). Because of the satellite orbit inclination and swath width there is no coverage pole-wards of 84°. There is SMMR data only every second day. Data were provided by the National Snow and Ice Data Center (NSIDC) as brightness temperatures in swath "projection" (Meier, 2008).

1.2 Description of the SSM/I and SSMIS instruments and data.

The SSM/I instruments onboard the Defense Meteorological Satellite Program (DMSP) are conically scanning instruments with 7 total power radiometers measuring at 19.35v, 19.35h, 22.2h, 37.0v, 37.0h, 85.5v, and 85.5h. The incidence angle is 53.1 degrees and the swath width on the Earth's surface is about 1400 km. There is no coverage pole-wards of 87 degrees. The different satellites and their operation periods are listed in Table 2. The SSM/I data (version 6) was purchased by EUMETSAT from Remote Sensing Systems (RSS) as antenna temperatures and converted to brightness temperatures using RSS software. The Remote Sensing Systems (RSS) SSM/I version 6 post processing includes geo-location correction, sensor calibration and quality control procedures, and inter calibration between the different satellites from overlapping periods. These procedures are documented in the RSS SSM/I User's Manuals (Wentz, 1991; Wentz, 1993; Wentz, 2006).

The SSMIS is a continuation of the SSM/I series of instruments onboard the DMSP satellites but with

The Cryosphere Discuss., doi:10.5194/tc-2016-34, 2016
Manuscript under review for journal The Cryosphere
Published: 17 March 2016
© Author(s) 2016. CC-BY 3.0 License.

an extension in the number of channels. SSMIS has 24 channels between 19 and 183 GHz. The 19 and 37 GHz channels which are used in the ESICR have identical frequencies on SSM/I and SSMIS. However, SSMIS has a swath width of about 1700km which gives near complete daily coverage of the Arctic Ocean. The SSMIS data are from the L2B near real time data-stream.

1.3 Meteorological data

The Numerical Weather Prediction (NWP) model meteorological data are used for reduction of the brightness temperatures for atmospheric noise with a radiative transfer model. European Centre for Medium-range Weather Forecast (ECMWF) ERA 40 data are used for the period from 1978 to 2002, and ECMWF data from the operational models are used from 2002 onwards. A description of the ERA 40 meteorological data archive and the reanalysis can be found in Kålberg et al. (2004). We use 6 hourly data at a resolution of 1.25 degrees.

1.4 MODIS data

The coarse resolution of the brightness temperature measurements gives rise to an additional uncertainty when sea ice concentration is reproduced at finer grid spacing. We call this smearing uncertainty and it is estimated using a smearing model (see section 2.9). High resolution ice concentration data are used as input to the smearing model. Cloud free MODIS scenes from the NASA image gallery archive (http://rapidfire.sci.gsfc.nasa.gov/cgi-bin/imagery/gallery.cgi) were selected manually for their different sea ice conditions: low concentration, medium and high concentration. Parts of the image with cloud cover were cut out. The band 1 (620 - 670 nm) brightness is high - typically greater than 220 for sea ice and less than 60 for open water. These two upper and lower values are used for scaling pixels between 100% and 0% ice concentration respectively. Pixels with intermediate brightness are assigned intermediate concentrations linearly. Brightness above 220 and below 60 is truncated to 100% and 0% respectively. The 250 m spatial resolution is re-sampled to 1 km pixel resolution.

1.5 Ice chart data for comparison

The operational sea ice charts from the National Ice Center (NIC) are a relatively independent source of ice information (not necessarily unbiased) for comparing to the sea ice concentration estimates. The

The Cryosphere Discuss., doi:10.5194/tc-2016-34, 2016
Manuscript under review for journal The Cryosphere
Published: 17 March 2016
© Author(s) 2016. CC-BY 3.0 License.

ice charts, intended for aiding navigation are produced on a regular basis covering all seasons, both Southern and Northern hemispheres and the time series cover the entire climate record period except for the period Dec. 1994 to Jan. 2003 in the Southern hemisphere where we have been unable to acquire digital ice charts.

Ice charts are produced manually on the basis of a multitude of satellite and reconnaissance data for ship navigation support. The ice charts are detailed manual interpretations of primarily satellite imagery and a subsequent mapping procedure is carried out by ice analysts. The ice charts are primarily used for strategic and tactical planning within the offshore and shipping community.

The more recent ice charts are based partly on satellite SAR data e.g. RADARSAT 1 since 1995 and ENVISAT since 2002, various scatterometers together with visual/infrared line scanners e.g. AVHRR, MODIS, OLS whenever possible for daylight and cloud cover conditions. Also the passive microwave data from SMMR and SMM/I used in this re-processing of ice concentrations have been extensively used for making the ice charts in particular before the launch of wide swath SAR instruments in 1995. In addition to the satellite data ice charts are based on information from ships and aircraft reconnaissance. The NIC ice charts are a weekly compilation of the ice conditions. The different sea ice categories are delineated by polygons and assigned a range of sea ice concentrations, thicknesses, type etc. found within the polygon in the ice chart. This information is represented on the satellite pixel grid by averaging the range of ice concentrations and other properties given within the polygon.

2.0 Methodology

2.1 Atmospheric noise reduction of the brightness temperatures using NWP data

Using an emission model, the brightness temperatures are corrected for the influence of water vapor in the atmosphere and open water surface roughness caused by wind shear. The emission model used for atmospheric noise reduction of the SMMR brightness temperatures, Tb, with NWP input is (Wentz, 1983):

$$Tb = f(Ts, u*, V, L, Ta) \quad (1),$$

where Ts is the physical surface temperature, U* is the sea surface wind friction velocity, V is the

The Cryosphere Discuss., doi:10.5194/tc-2016-34, 2016
Manuscript under review for journal The Cryosphere
Published: 17 March 2016
© Author(s) 2016. CC-BY 3.0 License.

integrated atmospheric water vapor column, L is the atmospheric liquid water column, and Ta is the surface (at 2 m) air temperature. A similar model is used for the SSM/I data (Wentz, 1997). Over areas with both ice and water the influence of open water roughness on the brightness temperatures and the ice emissivity is scaled linearly with the ice concentration. The emissivity of ice is given by standard tie-point emissivities and the total ice concentration is solved by iteration with a first guess of the ice concentration from the NASA Team algorithm (Cavalieri et al., 1984) with static tie-points. The correction procedure is described in detail in Andersen et al. (2006B). The NWP model grid points are co-located with the satellite swath data in time and space using linear interpolation and a correction to the brightness temperatures using Eq. 1 is applied. The potential inconsistencies between the ERA40 and the operational ECWMF models are minimized by the dynamical tie-point adjustment later in the processing and eventually the residual error is included in the error estimate.

The representation of atmospheric liquid water column in the NWP data is not suitable to use for brightness temperature correction. The data are therefore not corrected for the influence of atmospheric liquid water. Assuming a neutral atmospheric temperature profile, the wind speed at 10 m, given by the numerical weather prediction model, is converted to the surface friction velocity using the factor 0.047. The other NWP variables are used directly.

2.2 Dynamical tie-points

Tie-points are typical signatures of ice and open water which are used in the ice concentration algorithms as a reference. The tie-points are derived by selecting brightness temperatures from regions of known open water and ice.

During winter, in the consolidated pack ice well away from the ice edge, the ice concentration is very near 100 %. This has been established using high resolution SAR data, ship observations and by comparing the estimates from different ice concentration algorithms (Andersen et al., 2007). The apparent fluctuations in the derived ice concentration in the near 100 % ice regime are primarily attributed to snow/ice surface emissivity and temperature and atmospheric variability around the tie-point signature and only secondarily to actual ice concentration fluctuations. In the marginal ice zone at intermediate ice concentrations and over open water the atmospheric emission and wind shear and smearing dominates as error sources. There is no explicit correction for cloud liquid water and this is

The Cryosphere Discuss., doi:10.5194/tc-2016-34, 2016
Manuscript under review for journal The Cryosphere
Published: 17 March 2016
© Author(s) 2016. CC-BY 3.0 License.

an uncertainty source over both ice and open water. The fluctuations due to atmospheric and surface emission are systematic. In fact, different algorithms with different sensitivity to atmospheric and surface emission compute very different trends in sea ice extent on seasonal and decadal time scales (Andersen et al., 2007). This means that not only does the estimated sea ice extent have a climatic trend; also the atmospheric and surface constituents affecting the microwave emission are changing. In an attempt to compensate for the influence of these artificial trends the tie-points are derived dynamically using a window of width ± 15 days centered at the day of the actual sea ice concentration retrieval. It is assumed that ice concentrations greater than 95 % from the NASA Team algorithm (Cavalieri et al., 1984) are in fact a representation of near 100 % ice. The NASA Team algorithm has different sensitivities to artificial trends than the two algorithms (see section 2.3 below) used in combination here (Andersen et al., 2007). The ice tie-point is the mean value of these selected data points. The static NASA Team tie-points for SMMR are found in Gloersen et al. (1992) and for SSM/I the tie-points are found in Andersen (1998). Geographically, the sea ice tie-point is excluding data of both the SMMR and the SSM/I instruments pole-wards of 84° for consistency between the SMMR and SSM/I periods. The open water tie-point data were selected geographically along two belts on the northern and southern hemisphere respectively (between 53°N and 75°N and between 65°S and 80°S). A land mask including the coastal zone and sea ice maximum extent climatology ensures open water data only.

There is no attempt to compensate explicitly for sensor drift or inter-sensor calibration differences (even though the SSM/I data have been inter-calibrated) or possible biases in the NWP fields used for atmospheric noise reduction of the brightness temperatures. The dynamical tie-point method is in principle compensating for these problems in a consistent manner.

2.3 The ice concentration algorithm

The analysis of atmospheric sensitivity in Andersen et al. (2006B) showed that the Bootstrap frequency mode algorithm (Comiso, 1986; Comiso et al., 1997) had the lowest sensitivity to atmospheric noise at low ice concentrations. Furthermore, the comparison to high resolution SAR imagery in Andersen et al. (2007) indicated that among the algorithms using 19 and 37 GHz channels available on both SMMR and SSM/I - SSMIS, the Bristol algorithm (Smith, 1996) had the lowest sensitivity to ice surface

The Cryosphere Discuss., doi:10.5194/tc-2016-34, 2016
Manuscript under review for journal The Cryosphere
Published: 17 March 2016
© Author(s) 2016. CC-BY 3.0 License.

emissivity variability. In addition the Bristol algorithm had low sensitivity to atmospheric emission in particular at high ice concentrations.

Consequently, we use a combination of the Bristol algorithm and the Bootstrap frequency mode algorithm. The Bootstrap algorithm is used over open water and the Bristol algorithm is used over ice. At intermediate concentrations up to 40% the ice concentration is an average weighted linearly between the two algorithms. This hybrid algorithm is also used as the operational OSI SAF sea ice concentration algorithm.

2.4 The Bootstrap and Bristol sea ice concentration algorithms

The original Bootstrap sea ice concentration algorithm is a combination of two algorithms: the polarization mode which is used over ice and frequency mode which is used over open water (Comiso, 1986). Only the Bootstrap algorithm in frequency mode, the open water part, is used here. The algorithm assumes only two surface types: ice and open water. The linear relationship yields the following formulation for the total sea ice concentration, ic:

$$ic_{Bootstrap} = (Tb - Tb^W)/(Tb^I + Tb^W), \quad (2)$$

where Tb is the measured brightness temperature, Tb^W is the open water tie-point, and Tb^I is the ice tie-point.

The Bristol algorithm (Smith, 1996) is conceptually similar to the Bootstrap algorithm. In a three-dimensional scatter plot spanned by T_{19v}, T_{37v} and T_{37h} the ice points tend to fit a plane surface. The only difference to the Bootstrap algorithm is that instead of viewing the data in the T_{19v}, T_{37v} space, the Bristol algorithm views the data perpendicular to the data plane, i.e. in a transformed coordinate system:

$$\text{1. axis: } T_{37v} + 1.045T_{37h} + 0.525T_{19v}, \quad (3a)$$

$$\text{2. axis: } 0.9164T_{19v} - T_{37v} + 0.4965T_{37h}. \quad (3b)$$

The remaining analysis is identical to the Bootstrap algorithm.

The Bootstrap algorithm is used over open water and the Bristol algorithm is used over ice. At

The Cryosphere Discuss., doi:10.5194/tc-2016-34, 2016
Manuscript under review for journal The Cryosphere
Published: 17 March 2016
© Author(s) 2016. CC-BY 3.0 License.

intermediate concentrations up to 40% the ice concentration is an average weighted linearly between the two algorithms i.e.

$$ic = (1 - wc) * ic_{Bristol} + wc * ic_{Bootstrap} \quad (4a),$$

where

$$wc = (|t - ic_{Bootstrap}| + t - ic_{Bootstrap})/(2 * t) \quad (4b),$$

where t is the threshold of 40%.

2.5 The sea ice concentration uncertainties

The uncertainties described in the following sections are generally independent and the squared sum of the two estimated components of uncertainty is assumed to represent the total uncertainty squared. The tie-point uncertainty $\varepsilon_{\text{tie-point}}$, including residual atmospheric noise, sensor noise and ice surface emissivity variability, is derived from measurements as the first component of uncertainty. The representativeness error, $\varepsilon_{\text{smear}}$, is simulated using a model as the second component of uncertainty, i.e.

$$\varepsilon_{total}^2 = \varepsilon_{tie-point}^2 + \varepsilon_{smear}^2 \quad (5).$$

2.6 First component: instrument noise, algorithm and tie-point uncertainties

Both the water surface and ice surface emissivity variability and emission and scattering in the atmosphere affects the brightness temperatures and the computed ice concentrations. Different algorithms have different sensitivities to these surface and atmospheric parameters (Andersen et al., 2006B). Further, both the atmospheric and surface parameters affecting the ice concentration estimates have climatic trends (Andersen et al., 2007). To reduce the uncertainties due to atmospheric noise, the brightness temperatures are corrected using NWP data for atmospheric water vapor and open water roughness. The dynamical tie-points reduce the uncertainty due to the climatic trends in the atmosphere and on the ice surface on a hemispheric scale while regional trends may still exist. The remaining tie-point uncertainties are given as the spatial ice concentration standard deviation in regions with open water or 100% ice.

Random instrument noise also results in ice concentration uncertainties. The SSM/I instrument noise results in an ice concentration uncertainty of 1.4 % for the Bristol algorithm, and 1.7 % for the Bootstrap algorithm in frequency mode (Andersen et al., 2006A). Systematic sensor drift is critical issue for ice concentration algorithms using static tie-points. Here we use dynamical tie-points intended

The Cryosphere Discuss., doi:10.5194/tc-2016-34, 2016
Manuscript under review for journal The Cryosphere
Published: 17 March 2016
© Author(s) 2016. CC-BY 3.0 License.

for alleviating problems with sensor drift, inter-sensor calibration and climatic trends in ice surface emissivity and atmospheric emission, i.e. this method minimizes the uncertainties caused by sensor drift.

2.7 The geo-location error

Geo-location error - the geo-location error occurs when the satellite is not exactly oriented. Simulations show that because of the large footprints (see next section for footprint sizes) compared to the typical geo-location errors (about ±5 km, Hollinger et al., 1990) the ice concentration uncertainty due to geo-location errors is small and neglected here. Locally the geo-location errors may be significant but difficult to estimate.

2.8 Second component: the representativeness error

Footprint sizes for the channels used for ice concentration mapping range from about 50-70 km for the 19 GHz channels to about 30 km for the 37 GHz channels. Footprints of uneven size are combined in the algorithms when computing the ice concentration. The footprint ice concentration is represented on a predefined sampling grid. The ice concentration data are normally represented on a finer grid (typically 12.5 or 25 km) than the sensor resolution (30 to 70 km). This effect is called smearing. The combination of footprints of uneven size in the ice concentration algorithm results in an additional smearing effect. This we call the footprint mismatch error. The smearing and the footprint mismatch error cannot be estimated separately. However, the combined error can be estimated if all other error sources and the ice cover reference are known a priori. It can also be simulated using high resolution ice concentration reference data and a model for the satellite measurement footprint patterns. Here we use the model described in section 2.9.

2.9 Simulating the smearing uncertainty

The smearing simulation model uses high resolution brightness temperature input to compute the brightness temperatures as would be measured by the coarse resolution radiometers on board the satellite. The high resolution input is compared to the coarse resolution output and realizations of ice concentrations in the OSI SAF hybrid algorithm.

The Cryosphere Discuss., doi:10.5194/tc-2016-34, 2016
Manuscript under review for journal The Cryosphere
Published: 17 March 2016
© Author(s) 2016. CC-BY 3.0 License.

Reference SIC is cloud-free MODIS scenes re-sampled to 1 km x 1 km pixel size described in section 1.4. The MODIS intensity may vary slightly as a function of solar angle and snow type leading to uncertainties in the actual ice concentration. However, here it is regarded as the truth and it does provide a realistic spatial distribution of ice at the right scale for input to the model and as a reference for comparison. Each of these 1 km x 1 km ice concentration pixels is assigned a microwave brightness temperature using standard tie-points (Comiso et al., 1997) and linear mixing between 0 and 100%. For each 1 km x 1 km brightness temperature pixel elliptical Gauss-shaped antenna patterns (Drusch et al., 1999) are used to simulate brightness temperatures at 19v and 19h, 37v and 37h as it would be measured with SMMR and SSM/I - SSMIS on the satellite. The simulations of brightness temperatures are used as input to the CF and Bristol algorithms using standard tie-points. The resulting ice concentration estimate is then compared to the ice concentration reference sampled to different resolutions, i.e. 1, 5, 10, 12, 25 and 50 km (see table 2). The STD between the truth at a certain pixel resolution and the simulated satellite image is the smearing uncertainty. The smearing uncertainty is assumed uniform between 0% + $\varepsilon_{tiepoint}$ and 100% - $\varepsilon_{tiepoint}$. At 0% and at 100% it logically is zero. Table 2 shows the smearing uncertainty for the CF, the Bristol and the average OSI SAF STD of the difference at different grid resolutions. The final grid resolution is 10 or 12 km which means that the smearing uncertainty is 13% or 12% respectively. The smearing uncertainty is nearly the same for the CF and the Bristol algorithms.

The MODIS image used for estimating the smearing uncertainty is shown in Figure 1. The image has regions of open water, intermediate concentrations and of complete ice cover. The simulated SSM/I sea ice concentration using figure 1 as input to the OSI SAF algorithm is shown in figure 2.

2.10 The sea ice concentration uncertainty algorithm

The representativeness uncertainty is computed as a function of ice concentration using a model. The other error sources are computed using the hemispheric standard deviation of the measurements over open water and over near 100% ice respectively. The ice concentration algorithm provides ice concentrations which are greater than 100% and less than 0%. These unphysical concentrations are truncated in the processing. Therefore, we write the ice concentration, ic:

$$ic = (1 - \alpha(ic))water + \alpha(ic)ice \quad (6),$$

The Cryosphere Discuss., doi:10.5194/tc-2016-34, 2016
Manuscript under review for journal The Cryosphere
Published: 17 March 2016
© Author(s) 2016. CC-BY 3.0 License.

where ic is the ice concentration calculated by the algorithm and α as a function of ic is:

$$\alpha(ic) = \prod_0^1(ic)\, ic + H(ic-1) \quad (7),$$

where $\prod_a^b(x)$ is the Boxcar function and H(x) the Heaviside step function.

if ic≤0 then α=0
if 0<ic<1 then α=ic (8)
if ic≥1 then α=1

Using equation 2 and assuming the uncertainty for the ice and water part is independent this leads to a total tie-point uncertainty i.e

$$\varepsilon_{tie-point}(\alpha(ic)) = \sqrt{(1-\alpha(ic))^2\varepsilon_{water}^2 + \alpha^2(ic)\varepsilon_{ice}^2} \quad (9),$$

where $\varepsilon_{water} = \varepsilon(IC(P_{water}))$ (10),

and open water is determined by a monthly varying ocean mask, IC is the functional mapping of the ice concentration algorithm and P_{water} denotes the set of swath pixels for all swaths (used for calculating the daily product).

$$\varepsilon_{ice} = \varepsilon(IC(P_{NT>0.95})) \quad (11),$$

is the STD of the ice concentrations where the NASA team (NT) algorithm finds ice concentrations greater than 0.95.

Figure 3 shows the ice concentration uncertainty as a function of ice concentration. The total uncertainty squared is the sum of the different uncertainties squared (see eq. 4). The smearing uncertainty is zero for open water and for 100 % ice. At these two points on the curve there is only the tie-point uncertainty (including sensor and residual atmospheric noise) for open water and ice respectively. The smearing uncertainty reaches a maximum at intermediate concentrations between (0%+$\varepsilon_{tiepoint}$) and (100% - $\varepsilon_{tiepoint}$). Uncertainty for ice concentrations smaller than 0% and greater than 100% is the tie-point uncertainty.

The Cryosphere Discuss., doi:10.5194/tc-2016-34, 2016
Manuscript under review for journal The Cryosphere
Published: 17 March 2016
© Author(s) 2016. CC-BY 3.0 License.

Because the sea ice concentration is provided on a relatively fine grid of about 10 km and 12.5 km compared to the actual resolution of the sensor the smearing uncertainty is the component dominating the total uncertainty. When the grid resolution is comparable to the actual spatial resolution of the algorithm at 50 km the smearing uncertainty (see table 2) become comparable in magnitude to the tie-point uncertainty.

2.11 From level 2 swath projection data to level 3 daily grids to interpolated level 4 maps

The transition from level 2 swath projection data to level 3 and 4 daily predefined EASE and polar stereographic grids includes the gridding of the swath data, the filtering of coast line grid cells, maximum ice extent masking and spatial and temporal interpolation.

The time window of 24 hours is centered at 12:00 UTC. The ice concentration swath data is averaged for each grid cell using the weighting function:

$$weight = 1 - 0.3 * (dist/inflrad) \quad (12),$$

where *dist* is the distance between the data point centre and the grid cell centre and *inflrad* is the radius of influence (18 km). All data from overlapping missions are included in the gridding except the overlap between SMMR and SSM/I. Only the SSM/I data are used during the overlap of 1.5 months between SMMR and SSM/I.

2.12 Statistical filtering of ice concentration near the coastline

Due to the coarse resolution of the radiometers the data may be influenced by land up to 50 km from the coastline. The emissivity of land along the coastline is comparable to sea ice emissivity and much higher than water emissivity. This means that in the coastal zone if there is open water or intermediate concentrations the sea ice concentration will be overestimated. The statistical method which is described in Cavalieri et al. (1999) is used for filtering the ice concentration near the coast: For each grid cell along the coast the monthly mean and the minimum ice concentration is estimated using the 1985 SMMR and the 1992 SSM/I data. The minimum ice concentration is used instead of the estimated ice concentration if the adjacent non-coastal grid points are ice free.

The Cryosphere Discuss., doi:10.5194/tc-2016-34, 2016
Manuscript under review for journal The Cryosphere
Published: 17 March 2016
© Author(s) 2016. CC-BY 3.0 License.

2.13 Climatological maximum sea ice extent masking

Occasionally spurious sea ice is detected in open water regions far from the ice edge due to atmospheric noise affecting the ice concentration estimate. These spurious sea ice detections are masked out using the monthly maximum extent climatology by NSIDC (http://nsidc.org/data/smmr_ssmi_ancillary/ocean_masks.html). A zone of additional 100 km into the open water has been added to the maximum extent to ensure detection of real sea ice outside of the climatology.

2.14 Level 4: Gap filling by spatial and temporal interpolation

Only grid cells with missing data are filled with interpolated values in the level 4 processing and interpolated values are flagged. Daily data coverage is never complete and occasionally there are missing scan lines, missing orbits and the hole near the North Pole is never covered by the satellite. Interpolation is efficient in filling small gaps e.g. one or two missing scan lines but it is deceiving when large areas are missing and filled with interpolated values. To overcome this issue, yet implementing a general approach for all cases, both temporal and spatial interpolation is used. The interpolation on a given date D uses data from the day before and after, i.e. D-1, D and D+1.

The interpolated value at grid cell (i,j) for day *D* is given by:

$$X_{i,j}^{D} = K(w_{i,j}^{D-1}X_{i,j}^{D-1} + w_{i,j}^{D+1}X_{i,j}^{D+1} + \Sigma_{k,l}W^{D}(k,l;i,j)X_{k,l}^{D}) \quad (13),$$

where *X* is the sea ice concentration value and *K* is a normalizing factor given by:

$$w_{i,j}^{D-1} + w_{i,j}^{D+1} + \Sigma_{k,l}W^{D}(k,l;i,j) = 1/k \quad (14).$$

The spatial interpolation from neighbors of cell (i,j) in equation 6 is only using values from date *D*, while the temporal interpolation is only concerned with the value from the exact (i,j) cell but from dates *D-1* and *D+1*. This ensures that the interpolation will be efficient in the two following extreme scenarios: 1) In a region where we never have satellite observations e.g. the data coverage gap near the North Pole, the spatial interpolation term will be the only contribution. 2) Conversely, in the case of several missing swaths on day D only (nominal coverage on D-1 and D+1), the interpolated values will be computed from the previous and next days, taking advantage of the persistence of sea ice concentration over relatively short periods. The interpolation for intermediate cases (when both spatial

The Cryosphere Discuss., doi:10.5194/tc-2016-34, 2016
Manuscript under review for journal The Cryosphere
Published: 17 March 2016
© Author(s) 2016. CC-BY 3.0 License.

and temporal neighbors exist) is a compromise of those extreme situations.

In Eq. 6, the weighting parameters are computed as follows:

$$w_{i,j}^{D} = 1/(\sigma_{i,j}^{D})^2(2N_{max}+1) \quad (15)$$

$$W^{D}(k,l;i,j) = 1/(\sigma_{k,l}^{D})^2 \times exp(-0.5(\frac{\Delta(k,l;i,j)}{R_{i,j}})^2) \quad (16),$$

where σ is the standard deviation associated to each ice concentration estimate, Δ is the distance between a given (k,l) neighbor and cell (i,j) and *R* is an auto-correlation radius. The spatial interpolation weight is thus based on an isotropic Gaussian distribution, and almost all (>99.9%) of the interpolation weight is concentrated inside a [-3R;+3R] x [-3R;+3R] km^2 area, which translates into a [-N_{max};+N_{max}] x [-N_{max};+N_{max}] grid cells squared area. It was found by testing that *R* is proportional to the absolute latitude in degrees, i.e. *R* = latitude of (i,j).

For the SMMR which was operated every second day, the temporal interpolation is *D-2* and *D+2* instead of *D-1* and *D+1* for SSM/I.

3. Results and discussion

We compared the ESICR to sea ice charts for reference during the period from 1978 to 2009 on both hemispheres. There is a gap in the comparison on the southern hemisphere because we did not have access to ice charts between Dec. 1994 and Jan. 2003. The overlap period during July and August 1987 between the SMMR and the SSM/I instruments will be analyzed in more detail in section 3.2. The latter period from 2009 to 2014 is not compared to ice charts.

It is clear that ice charts are produced to support ship and offshore operations and not to monitor sea ice as a climate parameter. However, it is a relatively independent dataset with a long history, produced in a relatively consistent manner therefore we use it for comparison here.

3.1 The ice concentration comparison to sea ice charts

The entire period from 1987 to 2009 is covered by ice charts from the NIC on the northern hemisphere. For the southern hemisphere there is gap from Dec. 1994 to Jan. 2003. The ice charts and the sea ice climate record are gridded onto the 12.5 km EASE grid and compared. The total concentration in the ice chart is given as a range of sea ice concentrations describing the variability within each ice chart

The Cryosphere Discuss., doi:10.5194/tc-2016-34, 2016
Manuscript under review for journal The Cryosphere
Published: 17 March 2016
© Author(s) 2016. CC-BY 3.0 License.

polygon. For each ice chart concentration level (the total concentration) the deviation between ice chart and the ice concentration is computed and the bias and standard deviation is calculated for each concentration level. The bias and standard deviation are reported for ice (> 0% ice concentration), for water (0% ice concentration) and for both ice and water as a total.

The bias in ice concentration between the Northern Hemisphere National Ice Center ice charts and ESICR ice concentration is shown in figure 4. The ESICR ice concentration is higher than the ice chart over open water. This is due to the fact that the radiometer ice concentration is affected by atmospheric noise which increases the ice concentration above zero. The ice charts have a nominal value of zero over open water. Actually the mean open water ESICR ice concentration is zero. However, all negative ice concentration estimates are truncated to zero which leaves the small positive bias. Also the uncorrected noise from cloud liquid water, water vapor and wind over open water gives a positive bias in the ESICR ice concentrations. This positive bias is not present in the ice charts. The SMMR to SSM/I transition in 1987 is seen as a small increase in the open water bias because the SSM/I 19.35 GHz is affected more by water vapor than the 18.0 GHz SMMR instrument. Apparently not all the noise due to water vapor in the atmosphere is removed successfully in the atmospheric correction scheme. However, the higher noise level in SSM/I is quantified in the uncertainties. The ice bias has a clear seasonal cycle and a negative winter bias around 5% to 10%. The negative bias is caused by the truncation of the over 100% ice concentrations. The negative summer sea ice bias is sometimes reaching 20%. This is caused by anomalous sea ice emissivities during melt, the presence of melt-ponds, and perhaps an overestimation of the ice concentrations in the ice chart.

Figure 5 shows the northern hemisphere standard deviation of the difference between the ESICR and the national ice center ice charts. Both the standard deviation of open water and ice has a clear seasonal cycle with higher standard deviations during summer than during winter. The standard deviation of open water is decreasing during the latter part of the record. This could be a result of higher quality wind and water vapor data in the recent part of the ERA40 reanalysis and in the operational ECWMF model used since 2002.

Figure 6 shows the ESICR and national ice center difference for ice, water and both ice and water for

© Author(s) 2016. CC-BY 3.0 License.

the southern hemisphere. There were no digital ice charts available between Dec. 1994 and Jan. 2003. There is a small positive bias over open water due to the truncation of spurious sub-zero ice concentrations in the ESICR. The near 100% sea ice ESICR and NIC chart difference is negative around -10% during Antarctic winter. During the Antarctic summer the difference over ice is near -20%.

The standard deviation of the difference between the ESICR and the NIC ice charts shown in figure 7 is higher and has more inter-annual variability in Antarctica than in the Arctic except for the open water. The standard deviation of the difference for the open water case is between 0 and 5% from 2003 onwards.

3.2 The SMMR and SSM/I overlap

The overlap period between SMMR and SSM/I during July and August 1987 is short because 15 days prior and after the actual date is needed in order to establish the tie-points properly. Subtracting 15 days in each end of the overlap period leaves only a few days where the tie-points are fully established. Figure 8 and 9 show the overall bias between SMMR and SSM/I including the periods where tie-points are based on less than one month data, for NH and SH, respectively. On the Northern Hemisphere the overlap is during the sea ice minimum in 1987 which means that there are a limited number of ice data points.

The SMMR and SSM/I overlap period coincides with the ice maximum on the Southern Hemisphere which is ideal for comparison. However, the comparison is limited by the very short overlap just as for the Northern Hemisphere. Inspecting the differences geographically indicates that when environmental conditions have not changed significantly during SMMR and SSM/I passes then the SSM/I is slightly higher over open water while over ice it is close to neutral. The open water bias is probably due to the higher sensitivity of the 19.35 GHz channel on SSM/I to water vapor than the 18.0 GHz channel on SMMR.

3.3 Ice chart and ESICR comparison discussion

The NIC ice charts are produced manually on the basis of satellite and reconnaissance data for ship

The Cryosphere Discuss., doi:10.5194/tc-2016-34, 2016
Manuscript under review for journal The Cryosphere
Published: 17 March 2016
© Author(s) 2016. CC-BY 3.0 License.

navigation support and they do not contain estimates of uncertainty. However, the uncertainties in the ice charts from two other producers are relatively large with standard deviation of the difference between overlapping and coincident Greenland and Norwegian ice charts up to 30% ice concentration especially at intermediate concentrations (Breivik et al., 2015). Compared to microwave radiometer ice concentrations (the OSI SAF operational algorithm in Andersen et al., (2006B)) the ice concentration in Greenland ice charts is about 30% higher at intermediate concentrations. Trials with the ice concentration model described in section 2.9 shows that the estimates from most sea ice concentration algorithms including the Bootstrap and the Bristol is 1:1 proportional to the actual ice concentration and that there are very small differences between the overall response of different algorithms (ice concentration differences < 1% on 1000 km scale not including noise), i.e. different algorithms yield same ice concentrations given the same brightness temperature input. We did not find a similar investigation comparing NIC and other overlapping and coincident ice charts. However, we note that the methodology for making the Greenland, Norwegian and NIC ice charts is similar.

The bias between ice charts and radiometer ice concentrations at intermediate concentrations could be caused by two effects: 1) estimated radiometer ice concentrations are lower than real ice concentration for new ice and if the surface is melting or refrozen after melting and both new ice and melting refreezing is abundant in regions with intermediate concentrations, i.e. the radiometer is underestimating the real ice concentration 2) The ice charts ice concentration is a subjective estimate which is made for the safety of navigation and the overestimation of the ice concentration in the ice chart stem from “better-safe-than-sorry” practices within the ice charting community.

3.4 The ESICR metrics

In the following we are giving examples of the ESICR dataset for estimating sea ice climate statistics and trends. The applied climate period here is the full length of ESICR. First we show the long term trend in sea ice extent and secondly the trend in open water days in regions covered part of the season by sea ice. The examples are given for both the northern and the southern hemisphere.

Here the sea ice extent is defined as the area covered by sea ice within the ice edge. The ice edge is defined as the 30% contour and ice concentrations greater than 30% are considered as ice covered

The Cryosphere Discuss., doi:10.5194/tc-2016-34, 2016
Manuscript under review for journal The Cryosphere
Published: 17 March 2016
© Author(s) 2016. CC-BY 3.0 License.

while concentrations less than 30% are considered open water.

For the Arctic there is a negative trend in the monthly mean extent for all months of the year. The negative slope is largest in September -94 000±9700 km²/yr and smallest in May -32 000±4600 km²/yr. The monthly trends for the Arctic are shown in Table 3A.

For the Antarctic there is a positive trend in the monthly mean extent for all months of the year. The positive slope is largest in April, October and December at 33 000 km²/yr and the smallest in February 13 000±5400 km²/yr. The monthly trends for the Antarctica are shown in Table 3B.

Below we have looked at two periods of the 35 year ESICR: the entire 35 year period from autumn 1978 to the end of 2014 and the shorter recent 10 year period from 2004 to the end of 2014. The latter shorter period represents the period where most of the sea ice extent changes are taking place in both the southern and northern hemisphere.

Figure 10 shows the sea ice extent for the Arctic for both the long and the short record together with the September 2012 sea ice extent. The lower two panels are showing the seasonal variability of the sea ice extent and the long term mean monthly sea ice extent in March and in September which is the maximum and minimum extent respectively. September 2012 was the lowest sea ice extent on record in the Arctic since beginning of the satellite era. Over the 35 years of ESICR there is a negative trend in sea ice extent for all months of the year with the largest negative trend during the summer and the beginning of autumn (Jul-Oct) i.e. the third quarter of the year (Q3).

Figure 11 shows the sea ice extent for the Antarctic for both the long and the short record together with the September 2012 sea ice extent. The lower two panels are showing the seasonal variability of the sea ice extent and the long term mean monthly sea ice extent in March and in September which is the minimum and maximum extent respectively. The sea ice extent has experienced an overall positive trend around Antarctica especially downstream of the Weddell and the Ross Seas in the clockwise atmospheric circulation along the ice edge.

The Cryosphere Discuss., doi:10.5194/tc-2016-34, 2016
Manuscript under review for journal The Cryosphere
Published: 17 March 2016
© Author(s) 2016. CC-BY 3.0 License.

In order to determine the period of open waters for a given pixel, the annual spatial distribution of dates of freeze-up and break-up were calculated. The freeze-up date for a given point is defined as the date where the sea ice concentration climbs from below to above 30% and remains so for at least 5 days. The break-up date for a given point is defined as the date where the sea ice concentration falls from above to below 30% and remains so for at least 5 days.

The values for the ice concentration threshold and length of period were chosen by manually tuning for convergence: ice concentrations lower than 30% and periods less than 5 days were found to produce noise in the spatial distribution of freeze-up/break-up dates, which settles at the chosen values, though somewhat less so in the short 10 year record.

Since the sea ice does not retreat and expand completely every year, not all areas experience the same number of freeze-ups and break-ups over an equal period of years. Therefore, some regions may experience relatively few freeze-ups and break-ups, thus reducing the confidence in the trend of the region. As a consequence, only areas having experienced more than 6 freeze-ups/break-ups in each period are considered.

Figure 12 is showing the decadal trend in open water days in the Arctic region covered by sea ice part of the year. The open water days are calculated as the difference in days between freeze-up and break-up.

The trends in open water days are shown for both the long and the short climate record in figure 12 left and right, respectively.

Over the long record of 35 years the ice season has been shortened by at least 60 days in the Davis Strait and in large parts of the Barents Sea. The ice season has been shortened consistently all over the Arctic except in the Bering Strait region and the Greenland Sea. The shortening of the ice season is due both to a delay of the freeze-up and earlier breakup in combination (not shown). While this pattern is largely consistent for the short and the long periods in the Baffin Bay, and the Barents, Kara and Laptev Seas there are large differences in open water days trend in the Davis Strait and in the Beaufort

The Cryosphere Discuss., doi:10.5194/tc-2016-34, 2016
Manuscript under review for journal The Cryosphere
Published: 17 March 2016
© Author(s) 2016. CC-BY 3.0 License.

Sea and Bering Strait region. The short period has substantial negative trends in these regions (more than -15 days / decade) while the long period has positive trends. However, the statistical significance of the trends for the short period is lower than for the long period.

Figure 13 is showing the significance of the trends in number of open water days shown in figure 13 here as a test of the null-hypothesis, i.e. testing the probability of no trend. This means that a low probability indicates that the trend is in fact significant. It is noted that while the trend is significant in most regions for the long record the trends are not significant for the short record. This is due to the relatively short record of 10 years which is influenced by short term natural variability for example shifts in the mean location of the atmospheric pressure systems.

Figure 14 shows the decadal trend in the number of open water days around Antarctica in regions with a seasonal sea ice cover. As for the Arctic the open water days is calculated as the difference in days between freeze-up and breakup.

The trend in open water days is shown for both the long and the short record.

The significance of the trends in number of open water days per year is shown in figure 15 as a test of the null-hypothesis, i.e. testing the probability of no trend. It is noted that while the trend is significant in large regions in the Weddell Sea and in the Ross Sea for the long record the trends are more sporadically significant for the short record.

The negative trend on the long record in the Ross and in the Weddell Seas indicates that the ice is staying longer in these areas now than before. Along the ice edge in the Ross Sea, in East Antarctica, the Weddell Sea and in all of the Bellinghausen Sea there is a positive trend in the number of open water days. This means that the ice which is either advected into or formed in these regions is staying there for shorter time now than before and it indicates that these regions have experienced warming during the 35 years of the record. Even though there is an overall positive trend in the sea ice extent around Antarctica there is an indication that the warming is closing in on the pole.

The Cryosphere Discuss., doi:10.5194/tc-2016-34, 2016
Manuscript under review for journal The Cryosphere
Published: 17 March 2016
© Author(s) 2016. CC-BY 3.0 License.

4.0 Conclusions

A sea ice climate record covering the period from autumn 1978 to the end of 2014 has been produced based on past microwave radiometer data from SMMR, SSM/I and SSMIS. The climate record has been produced according to 4 principles to ensure consistency and to minimize the sensitivity to noise sources:

1) Finding algorithms with low sensitivities to geophysical noise. Two algorithms have been selected in combination based on the evaluation in Andersen et al., (2007), the Bristol over ice and the Bootstrap in frequency mode over open water. An independent evaluation of algorithms in Ivanova et al. (2015) pointed at the same two algorithms.

2) Regional error reduction correcting the brightness temperatures for water vapor in the atmosphere and wind over open water. The scheme described in Andersen et al. (2006B) is used to reduce the noise over both ice and water.

3) Calibrate the algorithms to the actual ice and water signatures and sensor drift using dynamical tie-points. The result of using dynamical tie-points has been demonstrated here at the transition from SMMR to SSM/I with satisfactory results. In addition, we do not see any jumps at sensor transitions or long term trends in the comparison to the independent ice chart dataset.

4) Quantify the residual uncertainties. A forward model for the residual uncertainties has been developed and applied. The total uncertainty as a combination of the tie-point variability and the representativeness uncertainty is a function of the ice concentration and it is applied on each individual measurement.

It is clear that the sea ice covers on both hemispheres have undergone large changes over the 35 year period. In the Arctic the linear trend at sea ice minimum month in September is -94 000 km²/yr.

Around Antarctica there has been an increase of the total sea ice extent during all months especially downstream of the Weddell Sea and in the Ross Seas. However, these extensions are relatively short

© Author(s) 2016. CC-BY 3.0 License.

lived meaning that the ice which is extending across the long term mean extent (primarily driven by advection) near sea ice extent maximum into the Atlantic and the Pacific ocean is removed by melt or advection relatively quickly. However, there are regional differences and the ice extent has decreased along the Antarctic Peninsula in the Bellinghausen Sea.

4.1 Future work

The sea ice climate record will be updated at irregular intervals. The next update is planned for autumn 2016. In addition, the daily OSI SAF sea ice concentration product and the ESICR is using the same algorithm and methodology with only minor differences.

In order to extend the sea ice climate record with past data it is being investigated if it is possible to retrieve the Nimbus 5 Electrically Scanning Microwave Radiometer (ESMR) 19 GHz swath data from 1972 to 1977. These single channel data are significantly different from SMMR and SSM/I - SSMIS data and a new sea ice algorithm would have to be used.

The next update will include development from the ESA sea ice climate change initiative project working towards improved sea ice climate record methodologies.

Acknowledgements

The work was completed with support from EUMETSAT's Ocean and Sea Ice Satellite Application Facility. The SMMR data were provided by the NSIDC, the SSM/I data by Remote Sensing Systems, and the numerical weather prediction model data by the ECMWF.

References

Andersen, S. Monthly Arctic sea ice signatures for use in passive microwave algorithms. Danish meteorological institute technical report 98-18, 1998. pp.29.

Andersen, S., L. Toudal Pedersen, G. Heygster, R. Tonboe, and L Kaleschke, Intercomparison of passive microwave sea ice concentration retrievals over the high concentration Arctic sea ice. Journal of Geophysical Research 112, C08004, doi10.1029/2006JC003543, 2007.

© Author(s) 2016. CC-BY 3.0 License.

Andersen, S., R. T. Tonboe and L. Kaleschke. Satellite thermal microwave sea ice concentration algorithm comparison. Arctic Sea Ice Thickness: Past, Present and Future, edited by Wadhams and Amanatidis. Climate Change and Natural Hazards Series 10, EUR 22416, 2006A.

Andersen, S., R. Tonboe, S. Kern, and H. Schyberg. Improved retrieval of sea ice total concentration from spaceborne passive microwave observations using Numerical Weather Prediction model fields: An intercomparison of nine algorithms. Remote Sensing of Environment 104, 374-392, 2006B.

Breivik, L.-A. S. Eastwood, J. Karvonen, F. Dinesen, A. Fleming, T. Hamre, L.T. Pedersen, R. Saldo, J.Buus-Hinkler, B. Hackett, F. Ardhuin, M. B. Jensen. Quality information doccument for OSI TAC sea ice products. Issue 1.10, pp. 62. MyOcean ref. MYOF-OSI-QUID-SEAICE, 09. March 2015.

Cavalieri, D. J., C. L. Parkinson. Arctic sea ice variability and trends 1979-2010. The Cryosphere 6, 881-889, 2012.

Cavalieri, D. J., P. Gloersen, and W. J. Campbell. Determination of Sea Ice Parameters with the NIMBUS-7 SMMR. Journal of Geophysical Research 89(D4), 5355-5369, 1984.

Cavalieri, D.J., C.L. Parkinson, P. Gloersen, J.C. Comiso, and H.J. Zwally. Deriving long-term time series of sea ice cover from satellite passive-microwave multi-sensor data sets. Journal of Geophysical Research 104(C7), 15803-15814, 1999.

Comiso J.C, D.J. Cavalieri, C.L. Parkinson, and P. Gloersen. Passive microwave algorithms for sea ice concentration: A comparison of two techniques. Remote Sensing of Environment 60, 357-384, 1997.

Comiso J.C. Characteristics of arctic winter sea ice from satellite multispectral microwave observations. Journal of Geophysical Research 91(C1), 975-994, 1986.

Comiso, J. C., R. Kwok, S. Martin, A. L. Gordon. Variability and trends in sea ice extent and ice

© Author(s) 2016. CC-BY 3.0 License.

production in the Ross Sea. Journal of Geophysical Research 116, C04021, doi:10.1029/2010JC006391, 2011.

Comiso, J. C., R. Kwok, S. Martin, and A. L. Gordon. Variability and trends in sea ice extent and ice production in the Ross Sea. Journal of Geophysical Research 116, C04021, doi:10.1029/2010JC006391, 2011.

Drusch, M., E. F. Wood and R. Lindau. The impact of the SSM/I antenna gain function on land surface parameter retrieval, Geophysical Research Letters 26(23), 3481-3484, 1999.

Gloersen, P., and F. T. Barath. A scanning multichannel microwave radiometer for Nimbus-G and SeaSat-A. IEEE Journal of Oceanic Engineering OE-2(2), 172-178, 1977.

Gloersen, P., W. J. Campbell, D. J. Cavalieri, J. C. Comiso, C. L. Parkinson, H. J. Zwally. Arctic and Antarctic sea ice, 1978-1987: satellite passive-microwave observations and analysis. NASA SP-511, Washington D. C., 1992.

Hollinger, J. P., J. L. Peirce, G. A. Poe. 1990. SSM/I instrument evaluation. IEEE Transactions on Geoscience and Remote Sensing 28(5):781-790, 1990.

Ivanova, N., Pedersen, L. T., Tonboe, R. T., Kern, S., Heygster, G., Lavergne, T., Sørensen, A., Saldo, R., Dybkjær, G., Brucker, L., and Shokr, M.: Inter-comparison and evaluation of sea ice algorithms: towards further identification of challenges and optimal approach using passive microwave observations, The Cryosphere, 9, 1797-1817, doi:10.5194/tc-9-1797-2015, 2015.

Källberg, P., A. Simmons, S. Uppala, and M. Fuentes. The ERA-40 archive. ERA-40 Project Report Series, ECMWF, Reading, 2004.

Meier, W. Scanning Multichannel Microwave radiometer (SMMR) reprocessing for EUMETSAT. OSI SAF Visiting Scientist Report. Pp. 9, 2008.

© Author(s) 2016. CC-BY 3.0 License.

Parkinson, C. L., and D. J. Cavalieri. Arctic sea ice variability and trends, 1979-2006, Journal of Geophysical Research - Oceans, 113, C07003, doi:10.1029/2007JC004558, pp. 28, 2008.

Rayner, N. A., D. E. Parker, E. B. Horton, C. K. Folland, L.V. Alexander, D. P. Rowell, E. C. Kent, and A. Kaplan. Global analysis of sea surface temperature, sea ice, and night marine air temperature since the late nineteenth century. Journal of Geophysical Research. 108 (D14). doi:10.1029/2002JD002670, 2003.

Smith, D. M. Extraction of winter sea ice concentration in the Greenland and Barents Seas from SSM/I data. International Journal of Remote Sensing 17(13), 2625-2646, 1996.

Tonboe, R., R.-H. Pfeiffer, and M. B. Jensen, E. Howe, and S. Eastwood. Validation report for Global sea ice concentration reprocessing. Products OSI-409, Osi-409a, OSI-430. V. 2.0, pp. 30. April 2015.

Wentz, F. J. A model function for ocean microwave brightness temperatures. Journal of Geophysical Research 88(C3), 1892-1908, 1983.

Wentz, F. J. A well-calibrated ocean algorithm for SSM/I. Journal of Geophysical Research 102(C4), 8703-8718, 1997.

Wentz, F. J. User's Manual, SSM/I Antenna Temperature Tapes, Revision 1. RSS Technical Report 120191, 1991.

Wentz, F. J. User's Manual, SSM/I Antenna Temperature Tapes, Revision 2. RSS Technical Report 120193, 1993.

Wentz, F. J. User's Manual, SSM/I Antenna Temperature, Version 6. *RSS Technical Memo 082806*, 2006.

The Cryosphere Discuss., doi:10.5194/tc-2016-34, 2016
Manuscript under review for journal The Cryosphere
Published: 17 March 2016
© Author(s) 2016. CC-BY 3.0 License.

Wentz, F. J., L. Ricciardulli, K. Hilburn, C. Mears. How much more rain will global warming bring? Science 10.1126/science.1140746, 2007.

Zhang, X. D., and J. E. Walsh. Toward a seasonally ice-covered Arctic Ocean: Scenarios from the IPCC AR4 model simulations, Journal of Climate, 19(9), 1730-1747, 2006.

The Cryosphere Discuss., doi:10.5194/tc-2016-34, 2016
Manuscript under review for journal The Cryosphere
Published: 17 March 2016
© Author(s) 2016. CC-BY 3.0 License.

Tables

Table 1. The different satellite missions carrying the SMMR, SSM/I and SSMIS instrument and the periods they cover.

Table 2. The STD of the difference between the simulated SSM/I - SSMIS satellite ice concentration and the reference ice concentration resampled to different grid resolutions in percent.

Table 3A. The mean monthly sea ice extent, long term trend and standard error of the trend in the Arctic. All figures are in millions of km².

Table 3B. The mean monthly sea ice extent, long term trend and standard error of the trend in the Arctic. All figures are in millions of km².

Sensor	Launch	End
Nimbus 7 SMMR	October 1978	August 1987
DMSP F8 SSM/I	June 1987	December 1991
DMSP F10 SSM/I	December 1990	November 1997
DMSP F11 SSM/I	November 1991	May 2000
DMSP F13 SSM/I	March 1995	November 2009
DMSP F14 SSM/I	May 1997	August 2008
DMSP F15 SSM/I	December 1999	-
DMSP F16 SSMIS	October 2003	-
DMSP F17 SSMIS	November 2006	-
DMSP F18 SSMIS	October 2009	-
DMSP F19 SSMIS	April 2014	-

Table 1. The different satellite missions carrying the SMMR, SSM/I and SSMIS instrument and the periods they cover.

	1 km	5 km	10 km	12 km	25 km	50 km
CF	18	16	14	13	10	7
Bristol	17	15	13	12	10	6
OSISAF	17	15	13	12	9	6

Table 2. The STD of the difference between the simulated SSM/I - SSMIS satellite ice concentration and the reference ice concentration resampled to different grid resolutions in percent.

The Cryosphere Discuss., doi:10.5194/tc-2016-34, 2016
Manuscript under review for journal The Cryosphere
Published: 17 March 2016
© Author(s) 2016. CC-BY 3.0 License.

Month	Mean [10^6 km²]	Trend [10^6 km²/yr]	Trend std err
Jan	14.641	-0.045	0.0040
Feb	15.505	-0.045	0.0043
Mar	15.620	-0.041	0.0042
Apr	14.772	-0.036	0.0048
May	13.403	-0.032	0.0046
Jun	11.899	-0.053	0.0044
Jul	09.667	-0.079	0.0060
Aug	07.458	-0.084	0.0083
Sep	06.881	-0.094	0.0097
Oct	09.053	-0.077	0.0089
Nov	11.138	-0.055	0.0052
Dec	13.241	-0.044	0.0043

Table 3A. The mean monthly sea ice extent, long term trend and standard error of the trend in the Arctic. All figures are in millions of km².

Month	Mean [10^6 km²]	Trend [10^6 km²/yr]	Trend std err
Jan	04.566	0.022	0.0092
Feb	02.911	0.013	0.0054
Mar	04.105	0.022	0.0072
Apr	06.860	0.033	0.0099
May	10.135	0.032	0.0089
Jun	13.229	0.029	0.0072
Jul	15.622	0.022	0.0055
Aug	17.129	0.022	0.0059
Sep	17.684	0.029	0.0089
Oct	17.278	0.033	0.0070
Nov	15.164	0.020	0.0065
Dec	09.932	0.033	0.0115

Table 3B. The mean monthly sea ice extent, long term trend and standard error of the trend in the Arctic. All figures are in millions of km².

The Cryosphere Discuss., doi:10.5194/tc-2016-34, 2016
Manuscript under review for journal The Cryosphere
Published: 17 March 2016
© Author(s) 2016. CC-BY 3.0 License.

Figures

Captions:

Figure 1. The 1 km cloud free MODIS image 3000 x 2200 km. The scene is situated north of McMurdo Station and east of the Ross Sea, Antarctica. Ice concentrations between 0% (black) and 100% (white). The scene is recorded at 03.30 UTC 2008/02/24 by the Aqua satellite. The scene center is at 69.5S, 165W.

Figure 2. The simulated ice concentrations using the SSM/I sensor specifications and the OSI SAF hybrid ice concentration algorithm and the data in figure 1 as input. Ice concentrations between 0% (black) and 100% (white).

Figure 3. The total uncertainty in blue and its two components the smear in red and the tie-point uncertainty in green as a function of ice concentration.

Figure 4. The Arctic ESICR - NIC ice chart difference for areas of ice in red, for areas of open water in black and the total, i.e. both ice and water, in blue.

Figure 5. The Arctic ESICR - NIC ice chart standard deviation of the difference for areas of ice in red, for areas of open water in black and the total, i.e. both ice and water, in blue.

Figure 6. The Antarctic ESICR - NIC ice chart difference for areas of ice in red, for areas of open water in black and the total, i.e. both ice and water, in blue.

Figure 7. The ESICR and NIC ice chart standard deviation of the difference around Antarctica. The blue curve is showing the total standard deviation of the difference for both areas of open water and ice. The red curve is for ice and the black curve is for water. No ice charts were available to us from 1994 to 2003.

Figure 8. The overlapping SMMR - SSM/I difference in the Arctic during summer melt. The blue curve is the total bias and the red curve is showing the ice bias.

The Cryosphere Discuss., doi:10.5194/tc-2016-34, 2016
Manuscript under review for journal The Cryosphere
Published: 17 March 2016
© Author(s) 2016. CC-BY 3.0 License.

Figure 9. The overlapping SMMR - SSM/I difference around Antarctica during austral winter. The blue curve is the total bias and the red curve is showing the ice bias.

Figure 10. The upper panel: the September 2012 sea ice extent in the Arctic compared to the mean extent for the long (left) and the short record (right) shown with the red line. The blue lines on either side of the mean extent line are the 5 and 95 percentiles of ice extent. The lower two panels are showing the annual cycle of sea ice extent. The shaded areas are the 5 and 95% percentiles. The lower panel is showing the long term (1978-2014) Arctic sea ice extent near its maximum in March and near its minimum in September.

Figure 11. The upper panel: the September 2012 sea ice extent in the Antarctic compared to the mean extent for the long and the short record shown with the red line. The blue lines on either side of the mean extent line are the 5 and 95 percentiles of ice extent. The lower two panels are showing the annual cycle of sea ice extent. The shaded areas are the 5 and 95% percentiles. The lower panel is showing the long term (1978-2014) Antarctic sea ice extent near its maximum in March and near its minimum in September.

Figure 12. Show the linear trend in open water days in the Arctic for the long record (1978-2014) to the left and the short record (2004-2014) to the right.

Figure 13. The probability that the trend in figure 12 is not significant (test of the null-hypothesis). A low value (< 5) indicates that the trend is significant.

Figure 14. Show the linear trend in open water days in the Antarctic for the long record (1978-2014) to the left and the short record (2004-2014) to the right.

Figure 15. The probability that the trend in figure 14 is not significant (test of the null-hypothesis). A low value (< 5%) indicates that the trend is in fact significant.

The Cryosphere Discuss., doi:10.5194/tc-2016-34, 2016
Manuscript under review for journal The Cryosphere
Published: 17 March 2016
© Author(s) 2016. CC-BY 3.0 License.

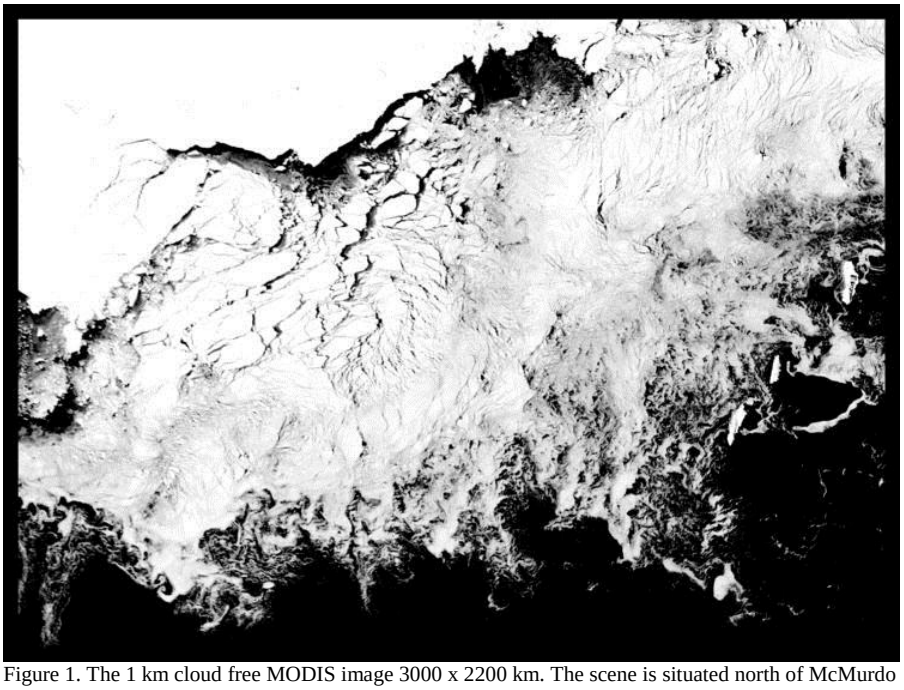

Figure 1. The 1 km cloud free MODIS image 3000 x 2200 km. The scene is situated north of McMurdo Station and east of the Ross Sea, Antarctica. Ice concentrations between 0% (black) and 100% (white). The scene is recorded at 03.30 UTC 2008/02/24 by the Aqua satellite. The scene centre is at 69.5S, 165W.

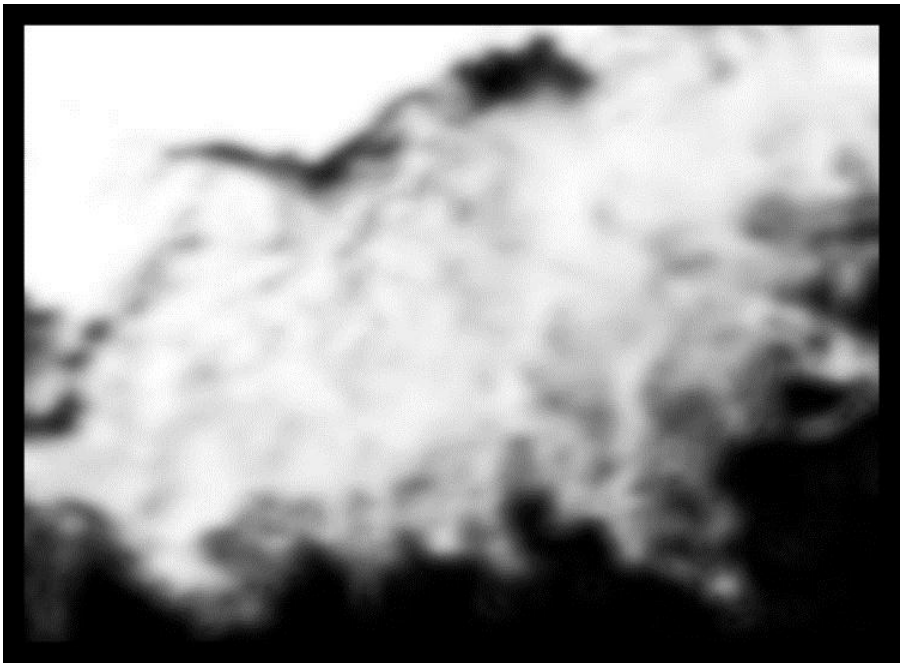

The Cryosphere Discuss., doi:10.5194/tc-2016-34, 2016
Manuscript under review for journal The Cryosphere
Published: 17 March 2016
© Author(s) 2016. CC-BY 3.0 License.

Figure 2. The simulated ice concentrations using the SSM/I sensor specifications and the OSI SAF hybrid ice concentration algorithm and the data in figure 1 as input. Ice concentrations between 0% (black) and 100% (white).

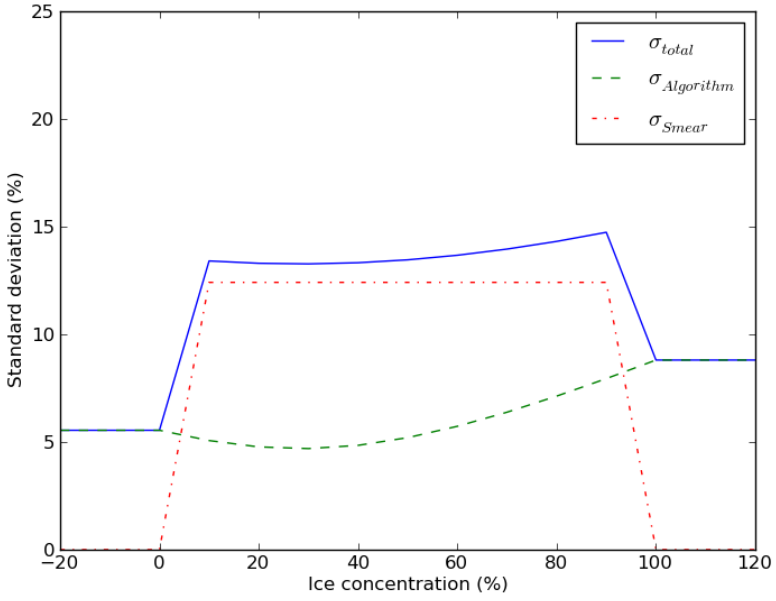

Figure 3. The total uncertainty in blue and its two components the smear in red and the tie-point uncertainty in green as a function of ice concentration.

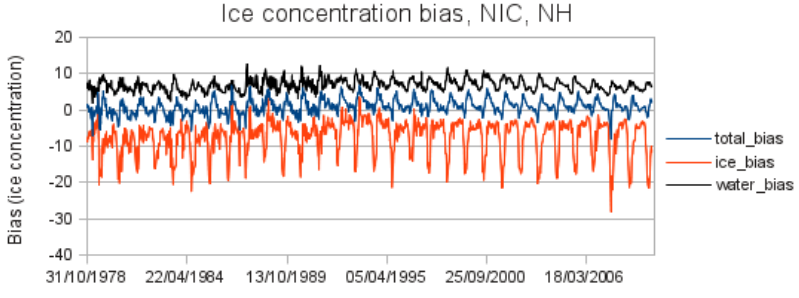

Figure 4. The Arctic ESICR - NIC ice chart difference for areas of ice in red, for areas of open water in black and the total, i.e. both ice and water, in blue.

The Cryosphere Discuss., doi:10.5194/tc-2016-34, 2016
Manuscript under review for journal The Cryosphere
Published: 17 March 2016
© Author(s) 2016. CC-BY 3.0 License.

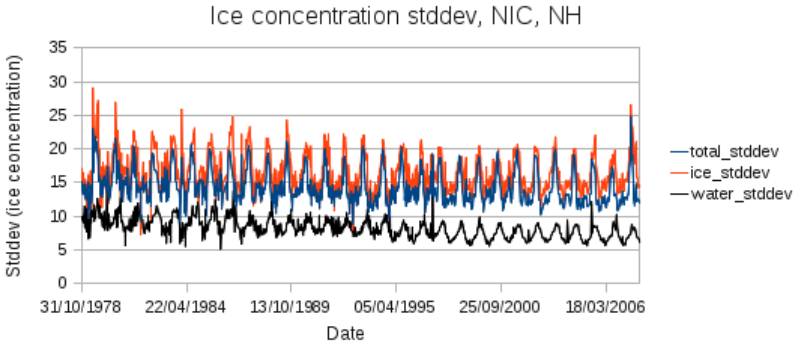

Figure 5. The Arctic ESICR - NIC ice chart standard deviation of the difference for areas of ice in red, for areas of open water in black and the total, i.e. both ice and water, in blue.

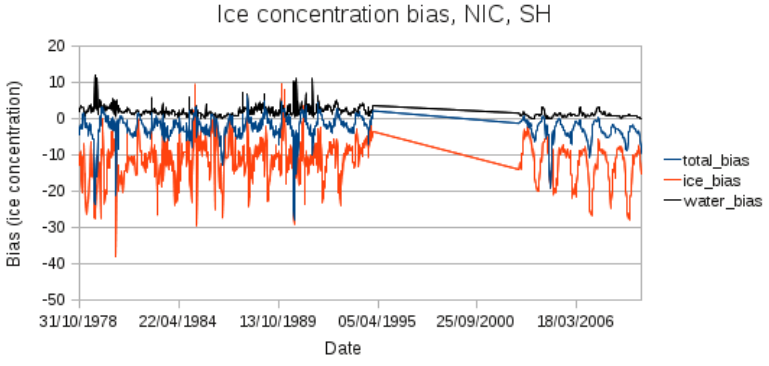

Figure 6. The Antarctic ESICR - NIC ice chart difference for areas of ice in red, for areas of open water in black and the total, i.e. both ice and water, in blue.

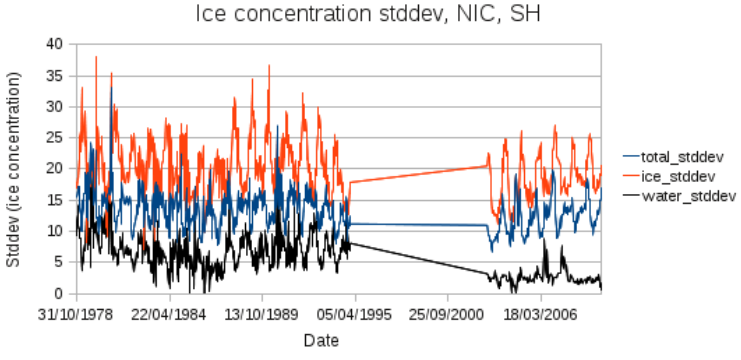

Figure 7. The ESICR and NIC ice chart standard deviation of the difference around Antarctica. The blue curve is showing the total standard deviation of the difference for both areas of open water and ice. The red curve is for ice and the black curve is for water. No ice charts were available to us from 1994 to 2003.

The Cryosphere Discuss., doi:10.5194/tc-2016-34, 2016
Manuscript under review for journal The Cryosphere
Published: 17 March 2016
© Author(s) 2016. CC-BY 3.0 License.

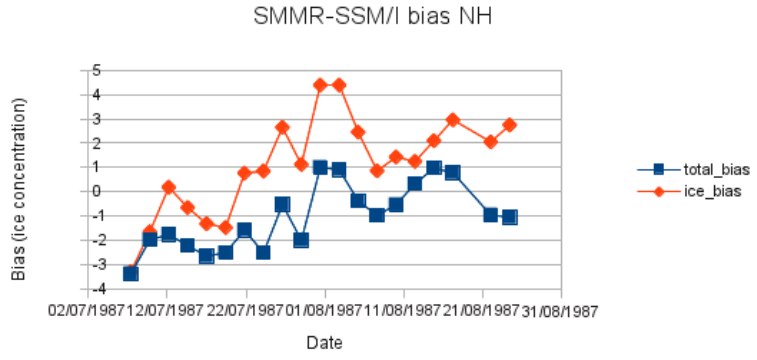

Figure 8. The overlapping SMMR - SSM/I difference in the Arctic during summer melt. The blue curve is the total bias and the red curve is showing the ice bias.

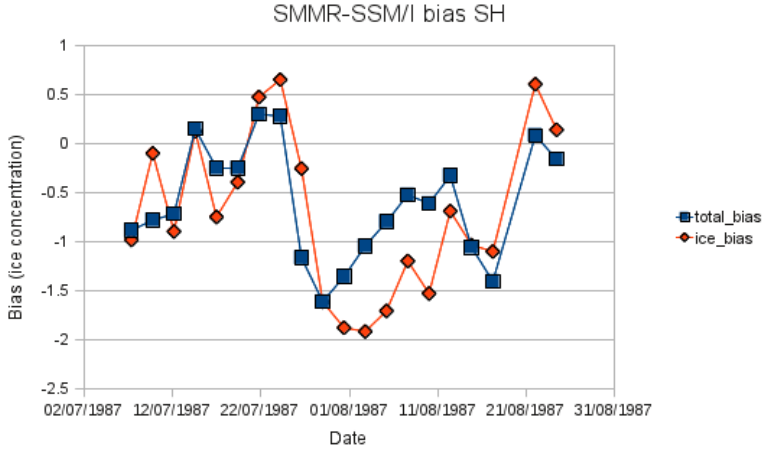

Figure 9. The overlapping SMMR - SSM/I difference around Antarctica during austral winter. The blue curve is the total bias and the red curve is showing the ice bias.

The Cryosphere Discuss., doi:10.5194/tc-2016-34, 2016
Manuscript under review for journal The Cryosphere
Published: 17 March 2016
© Author(s) 2016. CC-BY 3.0 License.

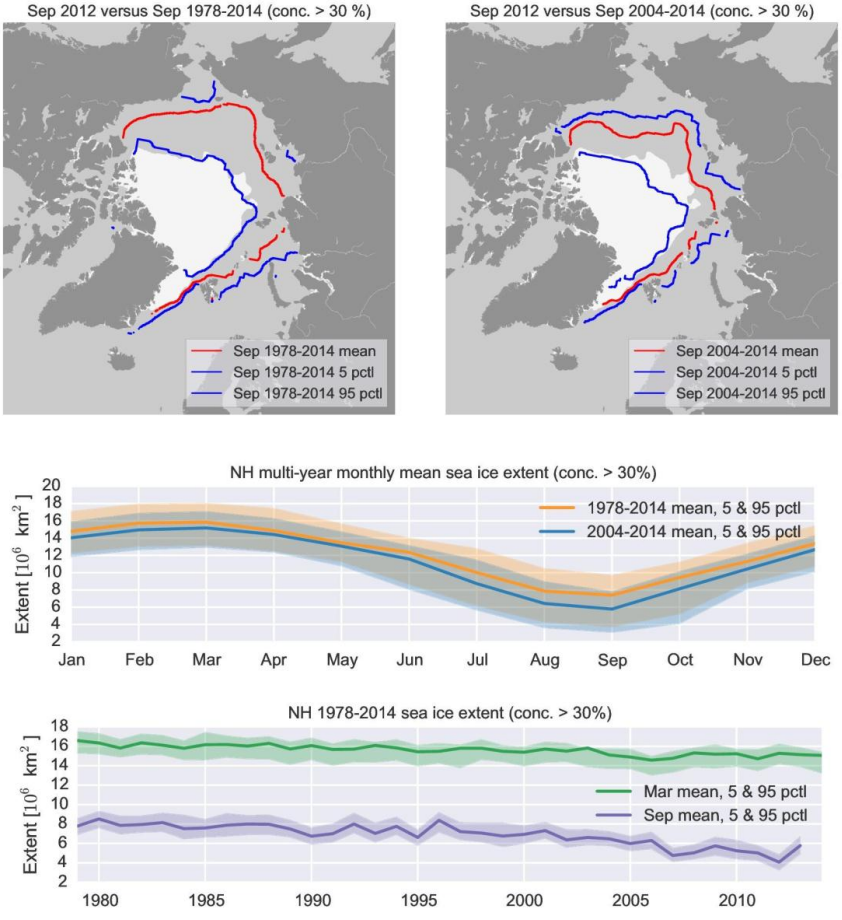

Figure 10. The upper panel: the September 2012 sea ice extent in the Arctic compared to the mean extent for the long (left) and the short record (right) shown with the red line. The blue lines on either side of the mean extent line are the 5 and 95 percentiles of ice extent. The lower two panels are showing the annual cycle of sea ice extent. The shaded areas are the 5 and 95% percentiles. The lower panel is showing the long term (1978-2014) Arctic sea ice extent near its maximum in March and near its minimum in September.

The Cryosphere Discuss., doi:10.5194/tc-2016-34, 2016
Manuscript under review for journal The Cryosphere
Published: 17 March 2016
© Author(s) 2016. CC-BY 3.0 License.

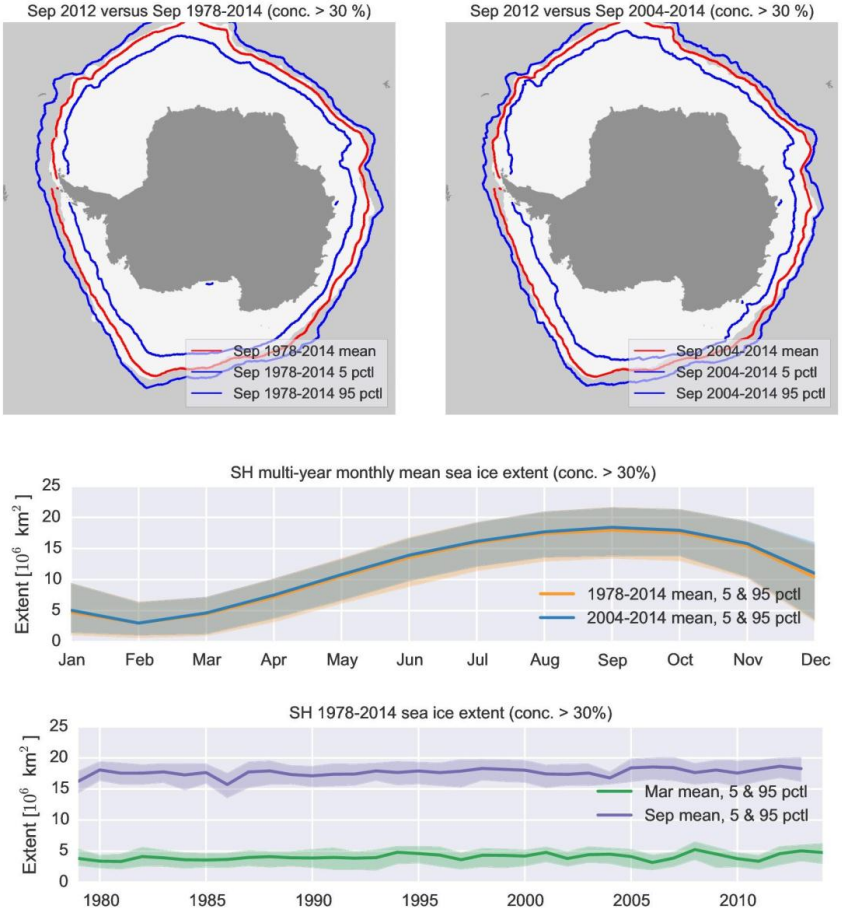

Figure 11. The upper panel: the September 2012 sea ice extent in the Antarctic compared to the mean extent for the long and the short record shown with the red line. The blue lines on either side of the mean extent line are the 5 and 95 percentiles of ice extent. The lower two panels are showing the annual cycle of sea ice extent. The shaded areas are the 5 and 95% percentiles. The lower panel is showing the long term (1978-2014) Antarctic sea ice extent near its maximum in March and near its minimum in September.

The Cryosphere Discuss., doi:10.5194/tc-2016-34, 2016
Manuscript under review for journal The Cryosphere
Published: 17 March 2016
© Author(s) 2016. CC-BY 3.0 License.

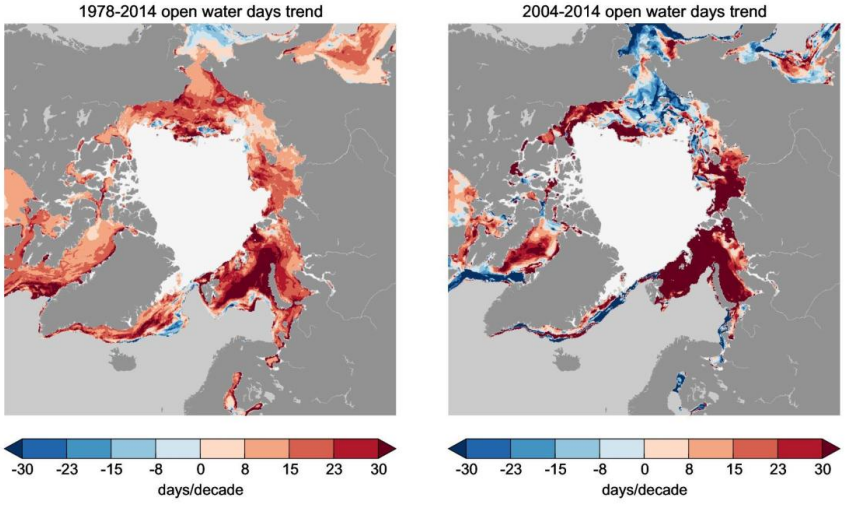

Figure 12. Show the linear trend in open water days in the Arctic for the long record (1978-2014) to the left and the short record (2004-2014) to the right.

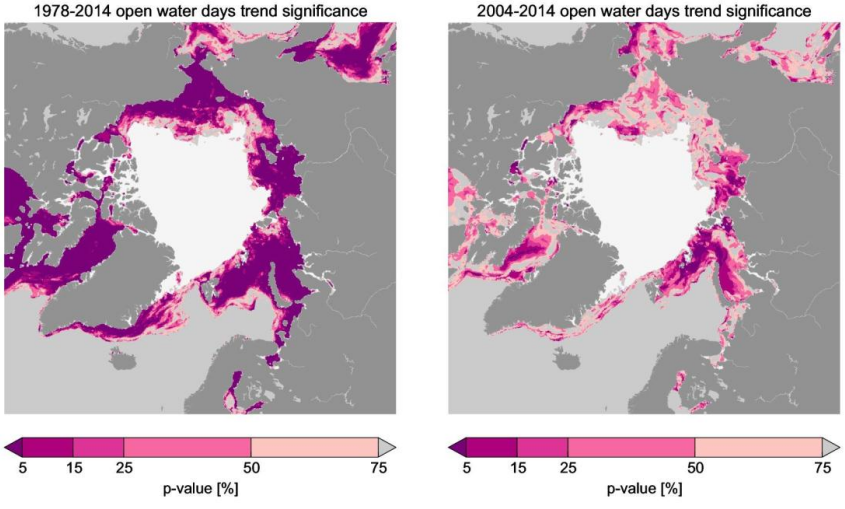

Figure 13. The probability that the trend in figure 12 is not significant (test of the null-hypothesis). A low value (< 5) indicates that the trend is significant.

The Cryosphere Discuss., doi:10.5194/tc-2016-34, 2016
Manuscript under review for journal The Cryosphere
Published: 17 March 2016
© Author(s) 2016. CC-BY 3.0 License.

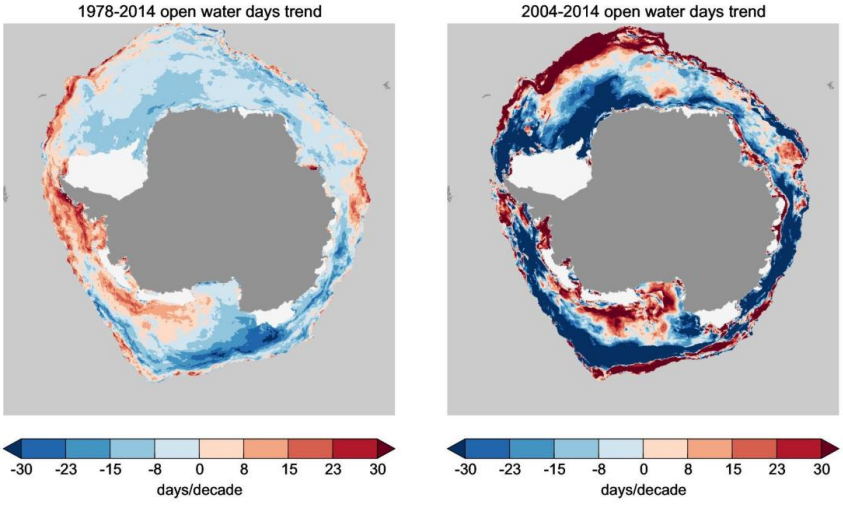

Figure 14. Show the linear trend in open water days in the Antarctic for the long record (1978-2014) to the left and the short record (2004-2014) to the right.

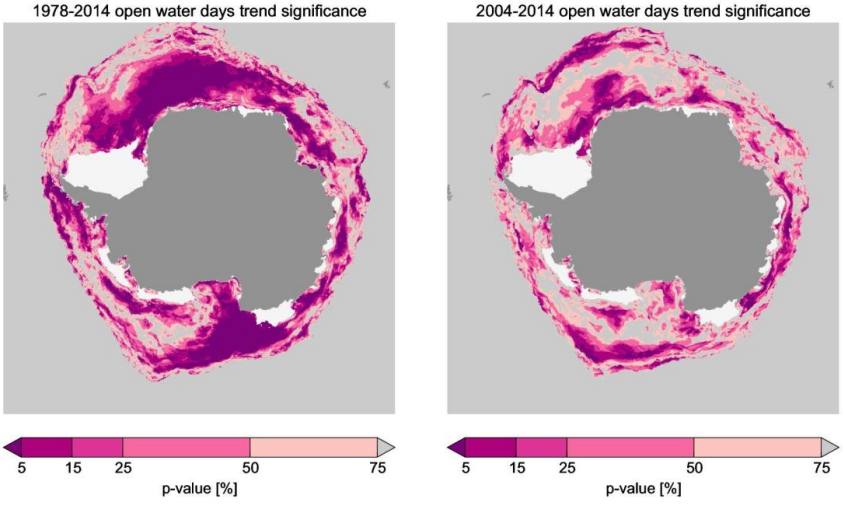

Figure 15. The probability that the trend in figure 14 is not significant (test of the null-hypothesis). A low value (< 5%) indicates that the trend is in fact significant.